

Progress in Lipid Droplet Simulations: How Polarizability Shapes Triacylglycerol Behavior in Bulk and Interfacial Environments

R. Jay Braun¹ and Jessica M. J. Swanson^{1*}

¹Department of Chemistry, University of Utah, Salt Lake City, UT 84112-0850, USA

*Corresponding author, j.swanson@utah.edu

Abstract

Triacylglycerols (TG) are the primary neutral lipids in lipid droplets (LDs), organelles responsible for lipid storage, metabolism, and signaling. Molecular dynamics (MD) simulations have provided valuable insight into LD structure, but fixed-charge force fields struggle to capture TG behavior across both hydrophobic cores and polar interfaces. Here, we develop and evaluate a polarizable TG model using the Drude2023 lipid force field and benchmark its performance against experimental measurements of bulk density, TG–water interfacial tension, core hydration, and monolayer expansion. The Drude model accurately reproduces the experimental properties and captures key monolayer features such as surface-oriented TGs (SURF-TGs) and chemically distinct membrane packing defects. Compared to fixed-charge models such as C36-standard and C36-cutoff, the Drude polarizable model is the only force field able to capture the dual nature of TG at polar-nonpolar interfaces like the LD monolayer and more homogeneous hydrophobic environments, like the LD core. However, C36-standard is consistent with the Drude results for the LD monolayer, while C36-cutoff is consistent with the decreased hydration in the LD core. Even with large applied surface tensions, C36-cutoff does not produce Drude-like LD monolayer properties. These results highlight the importance of dynamic polarizability and establish Drude2023 as a more reliable framework for simulating TG in heterogeneous systems like LDs.

Introduction

Lipid Droplets (LDs) are dynamic organelles that regulate the storage, distribution, and metabolism of neutral lipids, primarily triacylglycerols (TG) and sterol esters (SE), within cells. Unlike most organelles, which have bilayer membranes, LDs are surrounded by a phospholipid (PL) monolayer enriched with a dynamic array of proteins that are essential for metabolic processes such as lipolysis and lipogenesis (1–4). The unique physical properties of this surface play a central role in protein recruitment and the overall biology of LDs. Molecular dynamics (MD) simulations have played an important role in uncovering the behavior of the LD monolayer, providing molecular level insights into the dynamics and interactions that culminate in experimental properties and observations (5, 6). However, simulations are challenged by the timescales that can be reached, system sizes that can be represented, and forcefield accuracies. In this paper, we assess how current force fields capture TG behavior in the core and at the monolayer interface, highlighting deviations from experiment and how incorporating polarization can resolve these limitations.

The force field parameters for PLs have undergone more extensive optimization than those for neutral lipids, such as TG and SE lipids. Through numerous rounds of parameter optimization for multiple competing force fields models and against increasing amounts of guiding experimental data, MD studies of PL bilayers are now supported by increasingly robust PL parameter sets (7–11). Simulations of LDs have received less attention comparatively. Consequently, TG, the dominant neutral lipid in LDs, has only recently emerged as a focus of simulation studies (6, 12–14). To date, LD simulations have been particularly limited by the shortcomings of additive force fields (Fig 1), which require the definition of static partial charges. In reality, the polarizable glycerol moiety of TG, specifically the carbonyl and ester oxygens, exhibit environment-dependent charge distributions. In hydrophobic environments, such as the core of the LD near TG tails, lack of inducing interactions results in small effective partial charges, but at polar interfaces such as the surface of the LD monolayer, induced dipoles form, increasing the partial charges on the glycerol moiety. It is not possible for additive force fields to capture this dual nature, leading to an incomplete representation of TG behavior. Polarization is inherently a many-body effect, with each molecule both contributing to and being influenced by spatially varying and highly dynamic electrostatic interactions. Like other many-body interactions, such as dispersion interactions, polarization is implicitly mapped into effective pairwise potential parameters in additive force fields. Recent work has demonstrated the potential power of pairwise potentials in capturing some polarization effects when partial charges are properly scaled, as suggested by the electronic continuum formalism, (15–19) and ensuing halfway-charge (20, 21) and polarization consistent approaches (22). These methods have proven effective for homogeneous systems such as water, neutral molecules, and ionic liquids, but are typically unable to capture interfacial properties when the polarity of a molecule changes between bulk and interfacial contexts (23). Although using unlimited flexibility to fit all pairwise interactions for water via force-matching was impressively able to replicate behavior in bulk and at the air-water interface (24), more recent efforts on ionic liquids revealed clear differences between the pairwise and polarizable force fields (22, 25), highlighting the challenge of properly capturing bulk and interfacial environments.

This poses a challenge for LD simulations, where TG must be accurately modeled both in the largely hydrophobic LD core and at polar interfaces such as the PL monolayer where it may interact directly with water and/or polar protein residues. These limitations can impact the reliability of LD simulations and their interpretation. When developing parameters for a TG forcefield, several key experimental properties must be compared to (Table 1). The first is the bulk density of TG at about 0.9011 g/cm^3 (26). The second is the interfacial tension between bulk TG and water, which is approximately 30–32 mN/m (27, 28), representing the energy required to increase the surface area and reflective of the relative hydrophobicity of TG to polarity of water. The third is the hydration of a TG-LD core, which is not known experimentally, but is estimated to be 0.001 g/cm^3 based on studies of olive oil hydration (29).

The fourth and last is the area per lipid (APL) of the PLs in the LD monolayer, which is ~10-15% larger than that in bilayers of the same PL composition (30, 31). This increase has been attributed to the presence of TG molecules at the LD surface (Fig. 2), which integrate into the PLs, leading to a looser, more expanded monolayer. These properties are the consequence of the physical characteristics of TG in homogeneous, heterogeneous, bulk, and interfacial environments that should optimally be captured in TG models for reliable LD simulations.

Properties	Exp.	C36s	C36c/LJPM-r	MARTINI-s	Drude2023
V_{TG} (nm ³) (core density)	1.64 ^a	1.67	1.64-1.67	1.6	1.65
$\gamma_{TG/W}$ (mN/m) (interfacial tension)	30 – 32 ^{b,c}	17 ± 2	31-34	31.1	29.18 ± 1.8
A_{LD}/A_{BI} (Area per-PL ratio)	10 – 15% ^{d,e}	10.5%	3.3-3.5%	1.5%	10%
core hydration (g/cm ³)	0.001 ^f	~0.01	~0.001	N/A	~0.001

Table 1. Critical parameters for benchmarking TG forcefields comparing simulation and experimental values.

^aReference(26), ^{b,c}Reference(27, 28), ^{d,e}Reference(30, 31), ^fReference(29)

Previous studies using the CHARMM36-standard (C36s) force field modeled TG based on the DOPE (dioleoyl phosphatidylethanolamine) molecule by replacing the phosphate head group with an added oleate acyl tail. (32–34) While this model accurately reproduces density and the APL expansion of the LD monolayer compared to a bilayer of the same composition, it underestimates the TG-water interfacial tension at <18 mN/m and overhydrates the systems core approximately 10-fold relative to the hydration of bulk olive oil (Table 1). These issues stem from the overly polar glycerol group (Fig. 1), which was parameterized to work well for CHARMM36 DOPE PLs, but which does not accurately represent TG in a hydrophobic environment. Reduced-charge models, such as CHARMM36-cutoff (C36c) (12) or CHARMM36/LJPM-r (13) (we will only be referring to C36c since both forcefields are so similar), were developed address the low interfacial surface tension by reducing glycerol partial charges (Fig. 1) until the experimental TG-water surface tension was matched. However, these models do not capture the expansion of the LD APL relative to bilayer APL (Table 1). Rather the TG molecules become so hydrophobic that they are repelled from the interface and the APL remains largely unchanged. These limitations are shared by the course-grained (CG) models that have been employed for LD simulations. For example, the MARTINI-s force field for TG, constructed by replacing the PL head group with the PL chain, exhibits acceptable TG-water interfacial tension values but fails to show APL expansion (6). C36s remains the only forcefield to date, either all-atom or CG, capable of capturing LD APL expansion (Table 1), highlighting its utility despite trade-offs in overestimating core hydration or faithfully representing the bare-TG-water interfacial tension.

The above challenges underscore the potential need for polarizable force field parameters to accurately model TG molecules in the full range of LD contexts. Polarizable models allow the effective dipole to shift reactively and adapt to different interactions. In this study, we develop a TG parameter set using the Drude2023 lipid force field (35) and test the hypothesis that the limitations of existing force fields stem from a lack of polarizability. While Drude lipid forcefields has been validated for bilayers (35–37), this was the first test of its performance in PL monolayers and for TG. We assess its strengths and limitations, evaluating whether polarizability improves LD surface properties while identifying areas where further refinement is needed.

We find that the Drude-TG parameters quantifiably reproduce all the testable properties, with only a slight, but seemingly opposing underestimation of the water-TG interfacial tension (consistent with being too polar) and LD monolayer expansion (consistent with being too nonpolar). We also evaluated the Drude, C36s, and C36c parameter sets in LD systems under a range of applied surface tensions. Experimentally, LDs exhibit surface tensions in the range of ~1–3 mN/m, though this can likely increase during LD expansion or decrease during lipolytic reduction (30, 31, 38, 39). Protein association with the LD monolayer also modulates the effective surface tension and has been suggested to play a key role in the cytosolic direction of LD budding from the ER membrane. In simulations run with 0 mN/m applied surface tension, both the Drude and C36s models slightly underestimate the experimental monolayer expansion, driven by the spontaneous migration of surface-oriented triacylglycerols

(SURF-TGs) to the PL-water interface. These SURF-TGs stably occupy ~3–4% of the monolayer in Drude and C36s systems. In contrast, C36c significantly underestimates expansion, with minimal SURF-TG presence (~0–1%). At 3 mN/m applied surface tension, within the limits of biologically relevant surface tension, the Drude model expands to 14%, within the experimental range, with a monolayer SURF-TG content of ~5.5%. Meanwhile, C36s overexpands to ~23%, and C36c still underestimates expansion (6%) with little to no SURF-TG accumulation at the interface but increased tail intercalation from the LD core. Notably, C36c fails to match experimental expansion until the applied surface tension reaches ~10 mN/m, with SURF-TGs showing rapid exchange and limited stability at the interface. At higher surface tensions (5–10 mN/m), C36s increasingly overestimates expansion, consistent with the elevated static polarity of the TG-glycerol, while both Drude and C36c follow the experimental expansion isotherm. However, the physical and dynamic properties of the LD core and monolayer surface are quite different between the Drude and C36c forcefields. At both low and high surface tensions, the Drude model reproduces the extent of LD monolayer expansion observed experimentally, with more stable and long-lived SURF-TGs as opposed to the transient TGs and increased PL acyl defects observed with C36c under high surface tensions.

Notably, while SURF-TGs in Drude systems exhibited strong interactions with water, the core hydration remained near experimental values, highlighting the importance of polarizability in capturing these two properties. Additional surface characteristics, such as the number, size, and frequency of packing defects, revealed that Drude systems exhibited large, sustained TG-induced defects comparable to those in C36s, whereas C36c models primarily had PL-acyl defects. Furthermore, LD dynamics such as diffusion differed significantly between forcefields. Drude LDs exhibited the lowest core-TG diffusivity, with radial distribution functions (RDFs) revealing that induced dipole interactions between the Drude TG glycerol groups restricted molecular mobility. In contrast, C36c core-TG molecules displayed significantly higher diffusivity, highlighting the impact of reduced polarization on lipid dynamics. In summary, the Drude-TG parameter set provides a balanced representation of both bulk and surface properties in LD systems, outperforming the C36s and C36c models in key areas.

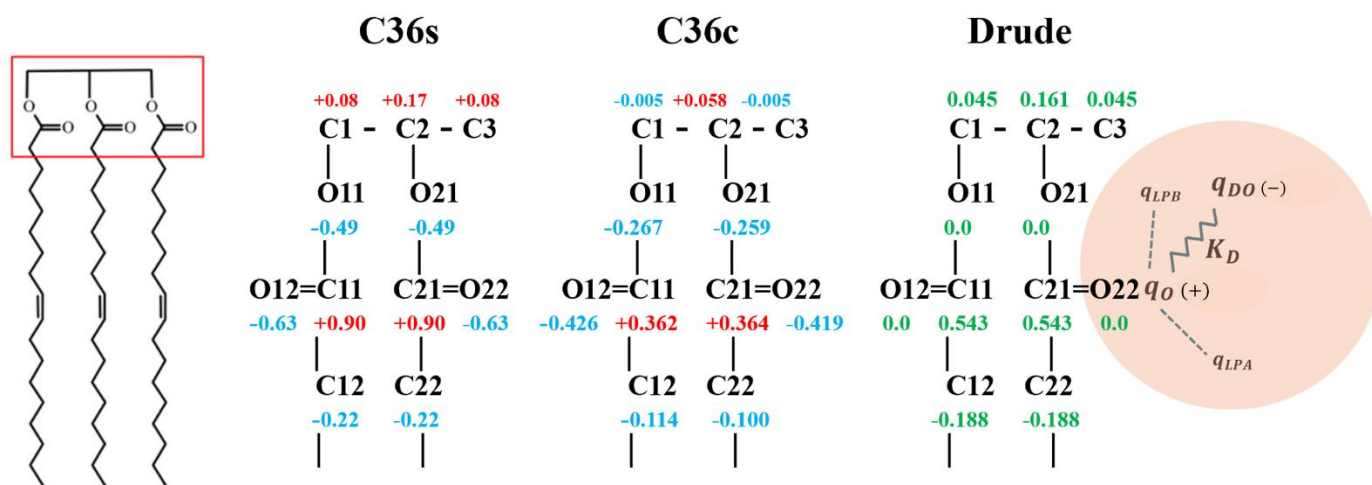


Figure 1. The charge distribution of the C36s, C36c and Drude2023 TG glycerol headgroups. The Drude model has a charge distribution (q) between each atom, a Drude oscillator tethered by a harmonic potential with a force constant (K_D), and appropriate virtual lone pairs (q_{LP}).

Methods

Drude triacylglycerol development: The Drude2023 lipid forcefield parameter set is available at reference (35). To create the TG parameters, we used a DOPE molecule (RESI DOPE) and replaced the phosphate group with an acyl tail. The glycerol group (RESI GLYC) has previously been explicitly parameterized (35) without being attached to a phospholipid, so using this group with acyl tails required no additional parameterization, as all bonds, angles, dihedrals, and non-bonded parameters were already available. The glycerol ester oxygens have no static charge, correcting the issue that was brought upon the C36s fixed charge parameters. Instead, a dipole is used to account

for the electrostatics dependent of the environment. The topology is available at github.com/swansongroup/Drude2023.

Interfacial tension with water interface:

The surface tension was calculated using the Kirkwood-Irving method (40):

$$\gamma = \frac{1}{2} L_z \left(P_{zz} - \frac{P_{zz} + P_{yy}}{2} \right) \quad (1)$$

Where γ is the surface tension in mN/m, L_z is the z-dimensional box length, P_{zz} is the normal component of the pressure tensor, and P_{yy} is the lateral component of the pressure tensor. The simulations for surface tension calculations were run on OpenMM 7.7 (41). The system, consisting of 400 TG molecules with a water (SWM4(42)) interface in the z-dimension, was set up using the Lennard-Jones PME (LJPM) (43) method for long-range dispersion interactions and a Drude Langevin integrator (41) with a 1 fs timestep, a temperature of 310 K, a Monte Carlo membrane barostat with a pressure of 1 atm, and friction coefficients of 5.0 ps⁻¹ for real atoms and 20.0 ps⁻¹ for Drude particles. After 100 steps of energy minimization, the system was equilibrated by assigning initial velocities from a Boltzmann distribution at 310 K. Drude virtual sites were computed, and the production run was performed. OpenMM does not currently allow for the calculation of pressure tensors necessary for the interfacial tension calculation, so a conversion to CHARMM (44) was needed. This required writing a separate velocity and coordinate file in DCD format every 10 picoseconds, using protocols shared with us by the authors of reference (35). With CHARMM scripting, we then ran single dynamics steps for each OpenMM output file, using the DCD velocity and coordinate files as inputs. Each of these steps calculated the atomic virial, providing the pressure tensors for each step of the simulation. These were then used as input for the Kirkwood-Irving equation. After 700 ns of simulation, it was apparent that the surface tension had equilibrated. The error was calculated using block averaging every 100 ns.

Simulation details:

LD systems were created in the same manner as our previous work (32, 45). Put concisely, bilayer systems were created using CHARMM-GUI membrane builder (46, 47) using POPC, and DOPE at an 88:47: molar ratio. This bilayer was used for benchmarking against the LD properties. The LD systems were built by separating the two leaflets of the bilayer and inserting a TG layer between them. The TG layer was constructed using Packmol (48), equilibrated for 50 ns in the NPT ensemble at 310 K ($\tau = 0.1$ ps) and a semi-isotropic Parrinello-Rahman barostat at 1 bar ($\tau = 2.0$ ps, compressibility = 4.5×10^{-5} bar⁻¹), and duplicated along the z-dimension to obtain the desired thickness. A 1-nm gap was initially maintained between the TG layer and the phospholipid leaflets, and any TG molecules within 2 Å of phospholipids were removed. The gap was further reduced through a 1 ns NPT simulation. Simulations for the LDs used GROMACS version 2021.4 (49) and the CHARMM36 (50) forcefield. Please refer to the previous work for more details (32, 45). From here, we then were able to convert the structure to the Drude OpenMM format using the conversion files provided from citation (35). GROMACS simulations were conducted at 310 K using the Nose-Hoover thermostat (51) with a 1 ps coupling time constant. Long-range electrostatic interactions were calculated using the Particle Mesh Ewald (PME) (52) algorithm with a 1.0 nm cutoff, while Lennard-Jones interactions were cutoff at 12 Å with a force-switching function applied between 8 and 12 Å. Pressure was maintained at 1.0 bar semi-isotropically using the Parrinello-Rahman (53) barostat with a compressibility of 4.5×10^{-5} bar⁻¹ and a 5.0 ps coupling constant. Hydrogen bonds were constrained using the LINCS (54) algorithm, and trajectories were recorded every 100 ps. For NPyT (constant particle number, normal pressure, surface tension, and temperature) simulations, the Berendsen (55) thermostat and barostat were used with the same parameters as before. For Drude simulations, the system was set up using the Drude2023 force field with LJ-PME for long-range dispersion interactions, using the simulation parameters from (35) as a reference. A DrudeLangevinIntegrator was used with a 1 fs timestep, 310 K temperature, and friction coefficients of 5.0 ps⁻¹ (real atoms) and 20.0 ps⁻¹ (Drude particles). A Monte Carlo Membrane Barostat maintained 1 atm pressure. The DCD trajectories and system state data were recorded every 1000 steps. Simulations were ran using OpenMM 7.7 (41).

Interdigitation analysis:

To quantify the intercalation of the core-lipid and PL components, we calculated interdigitation, following similar protocols as previous work (32, 56, 57). The degree of interdigitation between TGs and PLs was quantified using the overlap parameter $\rho_{ov}(z)$, defined from the TG and PL density profiles along the z-axis, $\rho_{TG}(z)$ and $\rho_{PL}(z)$ respectively:

$$\rho_{ov}(z) = 4 \frac{\rho_{TG}(z) * \rho_{PL}(z)}{(\rho_{TG}(z) + \rho_{PL}(z))^2} \quad (2)$$

The overlap parameter ranges from 0 to 1, where 0 indicates no overlap and 1 represents identical density distributions at a given z-position. The total interdigitation λ_{ov} was obtained by integrating the overlap parameter along the z-axis:

$$\lambda_{ov} = \int_0^L \rho_{ov}(z) dz \quad (3)$$

where L is the z-dimension of the simulation box. This metric quantifies the area common to the two density profiles.

SURF-TG identification and order parameter analysis:

SURF-TG were quantified in the same as in previous work (32). TG molecules that had all 6 glycerol oxygens above the midpoint of the center-of-mass of the PL acyl in the z-dimension, for the respective leaflet, were considered SURF-TG. To analyze the cosine alignment of the TG tails, terminal acyl tail carbons (C118, C218, C318) were determined by computing the vector between each tail atom and the TG headgroup center-of-mass. Cosine alignment with the LD normal was calculated as:

$$\cos\theta = \frac{v \cdot z}{|v|} \quad (3)$$

where v is the tail-to-headgroup vector, z is the bilayer normal, and $|v|$ is the vector magnitude. Frame-specific averages and standard deviations were computed separately for each leaflet and tail atom. The tail order parameters (58) for both SURF-TG and PLs were calculated with:

$$S = \left\langle \frac{3}{2} \cos^2(\theta) - \frac{1}{2} \right\rangle \quad (4)$$

with θ being the angle between the position vector of a carbon atom of an acyl chain bonded to a hydrogen with respect to the system normal. A larger value of S indicates increased ordering in the membrane. The brackets represent the ensemble average.

Packing defect analysis:

We refined a Cartesian-based algorithm to quantify lipid packing defects within monolayer leaflets, building on established methodologies (32, 59–61). Lipid atoms with z-coordinates above a threshold (Z_{thr}) were projected onto a 1 Å spaced x-y grid. The threshold was set to the average phosphorus atom z-position minus 2 nm, encompassing most leaflet atoms. van der Waals radii, defined from the forcefield parameter set, determined the overlap criteria between grid points and atoms. A grid point was considered occupied if its distance to an atom's center was less than the atom's radius plus ($\sqrt{3/2}\text{Å}$). Grid points overlapping with polar phospholipid headgroups were excluded from defect classification, while those overlapping with PL-acyl groups or neutral lipids were considered defects. Defects were identified using a depth-first search, clustering neighboring elementary defects. A defect size was assigned based on the number of elementary defects, measured in Å^2 . For a more detailed description of the defect analysis algorithm, please refer to the previous literature (32, 59–61). To obtain the number of defects per frame, we performed a block averaging over eight 100-ns intervals.

Mean squared displacement

The diffusion of lipids in our system was analyzed by computing the mean squared displacement (MSD) over time. Lipid molecules were tracked throughout the simulation, and their positions were recorded at each time step. The MSD was computed using the Einstein relation via MDAnalysis (62–64):

$$MSD(\tau) = \left\langle \frac{1}{N} \sum_{i=1}^N |r_i(t) - r_i(t_0)|^2 \right\rangle_{t_0} \quad (5)$$

where τ is the time lag, $r(t)$ is the position of lipid molecule i at time t , and N is the total number of lipids. To quantify three-dimensional diffusion, MSD was calculated using the full x, y, and z coordinates.

The lipid diffusion coefficient D was determined from the linear regime of the MSD curve using the Einstein relation for three-dimensional diffusion:

$$MSD = 6D\tau \quad (6)$$

where the slope of MSD versus τ provides a direct measure of D . This approach captures lipid motion in all spatial dimensions, allowing for a more comprehensive characterization of lipid dynamics within the system.

Results and Discussion

A fundamental limitation of fixed-charge force fields for heterogeneous, interfacial systems is their inability to capture environment-dependent variations in molecular charge distributions. For example, the C36s TG model—adapted from DOPE parameters, features a more polar glycerol moiety that is reflective of monolayer interfacial interactions, but increases hydration in the LD core relative to bulk olive oil hydration and underestimates the interfacial tension between pure TG and water (12, 32). To address the latter, modified force fields such as C36 LJPME-r and C36c reduced the partial charges on the glycerol group (Fig. 1), enhancing TG hydrophobicity (12, 13). While these adjustments improve the accuracy of interfacial tension predictions, they do not resolve discrepancies observed in LD monolayer expansion, illustrating a fundamental trade-off inherent in fixed-charge force field models. Accurately capturing LD monolayer expansion is critical, as it determines both the surface area and the structural landscape of packing available for protein binding. While C36c and C36-LJPME-r reproduce TG–water interfacial tension, this bare TG–water interface is questionably relevant to LD biology. Rather the behavior of TG in the LD core, PL monolayer, and with interacting proteins are most important for LD simulations. To test the value of polarizability in addressing the limitations of fixed-charge models, we developed TG parameters within the polarizable Drude2023 lipid force field and benchmarked them against the four key experimental observables: TG–water interfacial tension, bulk TG density, LD core hydration, and LD monolayer expansion relative to bilayers. We also compared the resulting LD physical properties across different force fields to assess their distinct behaviors and implications for modeling.

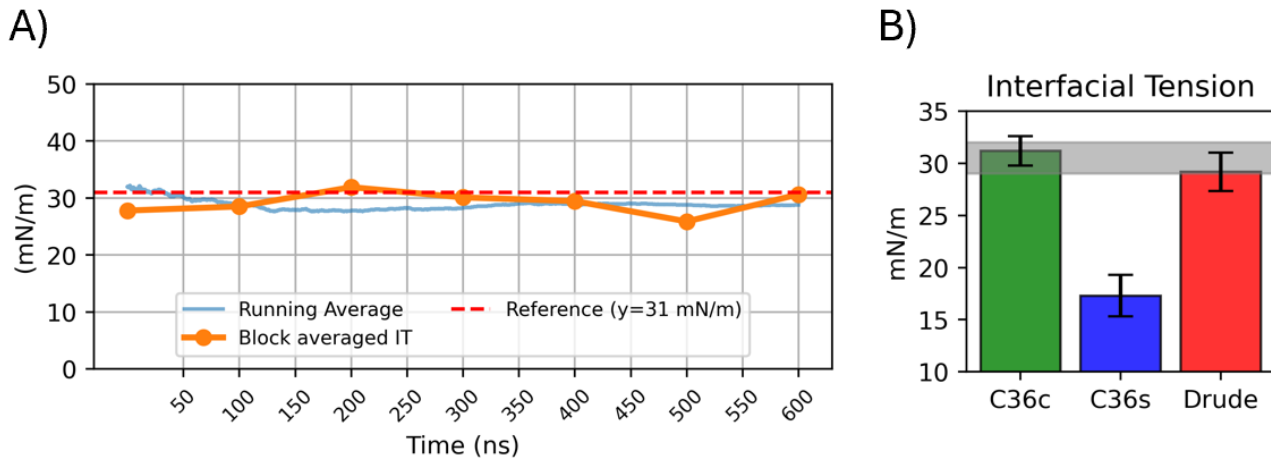


Figure 2. (A) Time averaged interfacial tension of the Drude TG at the water interface averages 29.18 mN/m. (B) The comparison of interfacial tensions among the C36c, C36s, and Drude systems.

Bulk and Interfacial Properties: Experimentally, the bulk TG density is approximately 0.9001 g/cm^3 (26), similar to the Drude2023 model at $0.8882 \text{ g/cm}^3 \pm 0.004$ (Table 1). At the water/TG interface the Drude2023 system has an interfacial tension of $29.18 \text{ mN/m} \pm 1.8$ (Fig. 2 A-B), near the experimental value of 30-32 mN/m. This result is significantly closer than the $\sim 17 \pm 2 \text{ mN/m}$ observed with the C36s force field (12), but slightly lower than that for C36c, which was parameterized to reproduce this property (12).

Unlike bilayers, LD monolayers are less densely packed with phospholipids, experimentally shown to incorporate only $\sim 87\text{--}90$ lipids per unit area compared to 100 in bilayers, corresponding to a $\sim 10\text{--}15\%$ increase in APL (30, 31). This expansion has been consistently observed in experimental systems of equivalent composition and is widely attributed to the interdigitation of neutral lipids, particularly TG molecules, into the monolayer interface (Fig. 3A). The presence of SURF-TG has been documented in prior experimental studies (28, 65, 66), where there has been reported measurable surface fractions (2–4%) of TGs in lipoprotein emulsions, supporting the notion that TGs can reside at lipid interfaces rather than being confined to the hydrophobic core. Additionally, while bilayers at equilibrium exhibit surface tensions near 0 mN/m, LDs consistently display surface tensions in the range of 1–3 mN/m (30, 31), further supporting the functional relevance of interfacial TGs and their role in modulating lipid packing at the monolayer surface. To assess how well different force fields reproduce this behavior, we compared the APLs of LD monolayers and bilayers simulated at 0 mN/m surface tension (Fig. 3C). All LD systems showed increased APL relative to their bilayer counterparts, consistent with interdigitation of TG molecules. At 0 mN/m, the Drude and C36s models exhibited comparable monolayer expansions of $\sim 10\%$ and 10.5% , respectively, whereas the C36c LD showed only a 3.5% increase—driven primarily by TG tail intercalation but reflecting a more compact monolayer with limited penetration of TG headgroups at the interface.

Monolayer Expansion and Surface Tension To evaluate performance under differing physiologically relevant surface tensions, we applied 3 mN/m in simulations using the NPyT ensemble. Under this condition, the Drude LD expanded to 14%, aligning more closely with experimental expectations. In contrast, C36s systems expanded to $\sim 23\%$, consistent with the statically polar glycerol promoting TG accumulation at the interface. The C36c LD expanded by just 6% under 3 mN/m, undershooting the experimental range. However, increasing the applied surface tension to 10 mN/m caused the C36c monolayer to expand by $\sim 16.5\%$, matching experimental values and suggesting that higher tension is necessary for this force field to reproduce LD-like monolayers (Fig. 3C). Based on these results, one could argue that Drude performs best near 3 mN/m, C36s between 0–1 mN/m, and C36c at 10 mN/m. For most of our comparative analysis we focus results at 0 mN/m for two key reasons: (1) to enable direct comparison with standard NPT simulations, which remain the field’s standard and avoid reliance on the Berendsen barostat or complications arising from artificially imposed surface tension; and (2) to leverage a larger pool of available long-timescale simulation data. For C36c, we additionally analyze results at 10 mN/m, where its APL values better match experiment, to determine whether this condition yields a more accurate representation of LD monolayers.

Finally, we evaluated the monolayer expansion behavior of each model against experimental isothermal expansion data reported experimentally (30), which describe APL changes under increasing applied tension relative to the 0 mN/m baseline (Fig. 3B). Although the larger surface tensions are not likely biologically relevant, this is one of the few experimental comparisons available, and it captures how readily the monolayer responds to growth conditions. Among the models, C36s displayed the steepest expansion reflecting the strong surface activity of its statically polar TG molecules. In comparison, the C36c and Drude models also exhibited steeper slopes, but are much closer to the experimental trend and thus more accurately capturing the extent of monolayer expansion under applied tension.

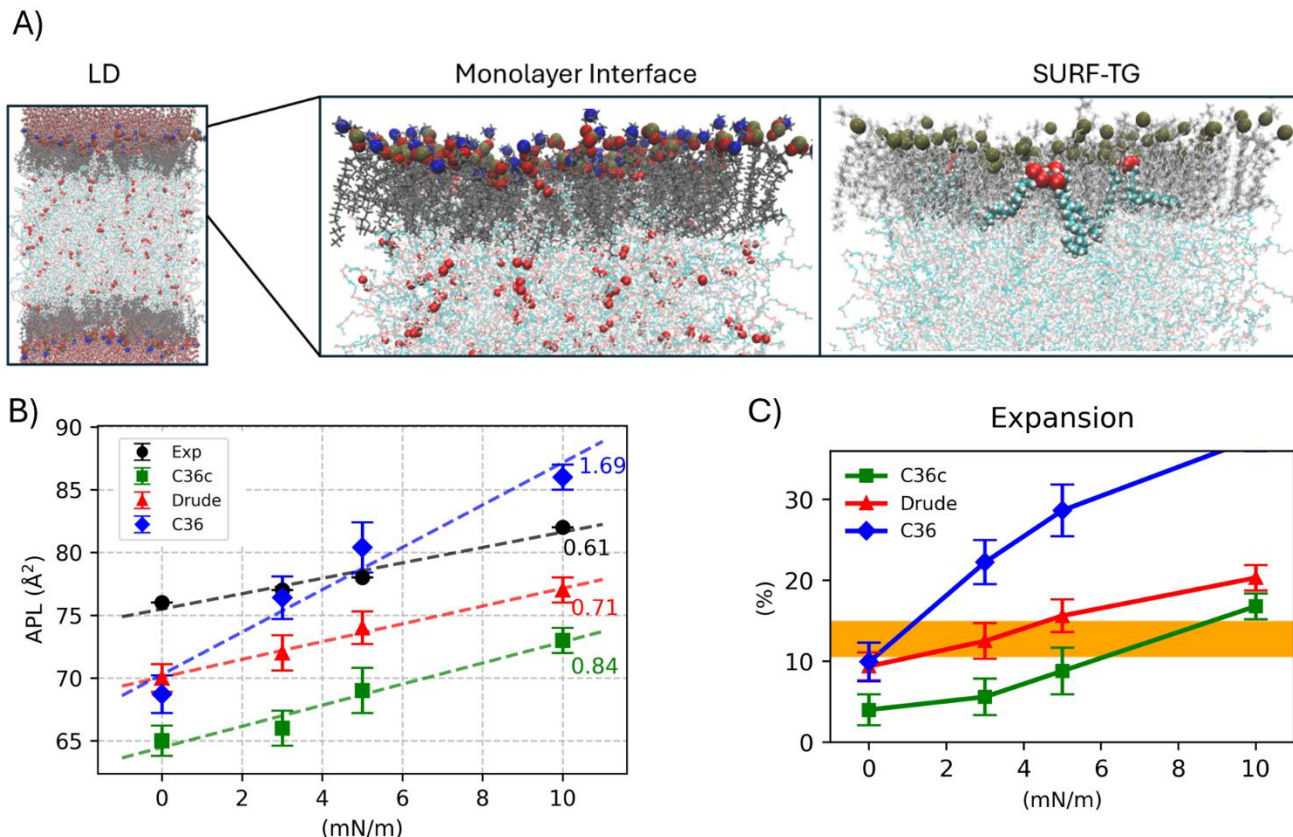


Figure 3. (A) LD trilayer systems with SURF-TGs. (B) Isothermal expansion of LD monolayer with applied surface tension determines that Drude (red line) has the most similar slope to experimental (black line). (C) Expansion compared to bilayers of identical composition.

Neutral Lipid Interdigitation: Expansion of the LD monolayer is strongly influenced by interdigitation of neutral lipids into the PL monolayer, which involves both tail intercalation and surface-oriented intercalation (e.g., SURF-TG). We quantified this behavior using the interdigitation metric λ_{OV}^{Lipid} (see Methods) measured in nanometers, which provides a consistent and informative measure of the overlap between PLs and neutral lipids. Strong interdigitation (λ_{OV}^{SURF}) was defined as cases where all six TG oxygen atoms lie above the average z-position of the PL acyl tail center of mass (Fig. 4A), while weak interdigitation (λ_{OV}^{WEAK}) captures overlap between TG tails and PL tails.

The Drude LD systems required longer to equilibrate than C36s or C36c. In our initial non-equilibrated Drude simulation, which starts with no overlap, λ_{OV}^{SURF} gradually increased to ~ 1 nm over 2.5 μ s (SI Fig. 1), corresponding to a stable SURF-TG population of ~ 3.5 -3.9% in the monolayer. To confirm convergence, we tested several control protocols. In one, the Drude LD was initialized at 20 mN/m surface tension, then reduced to 0 mN/m after 100 ns. In another, the system was heated to 315 K for 50 ns and cooled to 310 K. In both cases, λ_{OV}^{SURF} reliably converged to ~ 1 nm (SI Fig. 1), confirming consistent equilibrium behavior. Furthermore, converting a C36s LD that had been equilibrated over 1300 ns ($\lambda_{OV}^{SURF} \approx 1$ nm) to Drude parameters preserved this interdigitation level over time (Fig. 4B), but with smaller fluctuations. In contrast, the C36c systems exhibited minimal SURF-TG interdigitation. When initiated from a non-equilibrated state, λ_{OV}^{SURF} plateaued at just ~ 0.1 nm (SI Fig. 1). Even when initialized from the pre-equilibrated C36s system ($\lambda_{OV}^{SURF} \approx 1$ nm), SURF-TGs were expelled back into the core within 240 ns, with λ_{OV}^{SURF} declining to 0 nm (Fig 4B). Only under applied tension (10 mN/m) did C36c maintain partial interdigitation, reaching λ_{OV}^{SURF} values of ~ 0.3 -0.4 nm (SI Fig. 1).

These results highlight SURF-TG as a key determinant of monolayer expansion, even in the absence of externally applied surface tension, emphasizing that interfacial remodeling can arise from intrinsic molecular interactions

alone. In Drude simulations, TG headgroups gradually partition to the monolayer, stabilizing at an inherent equilibrium fraction of ~3–4%, independent of initial surface tension. C36s produces a similar SURF-TG fraction (~4%), in ~800 ns relative to Drude's 2.5 μ s. C36c systems show reduced SURF-TG populations (~1.5% at 10 mN/m), consistent with limited interfacial stabilization. To quantify the correlation between interdigitation and monolayer expansion, we computed Pearson correlation coefficients between λ_{OV}^{SURF} and APL across systems. Both Drude and C36s models showed strong correlations (0.81 and 0.80, respectively), indicating that enhanced TG headgroup interdigitation promotes monolayer expansion (Fig. 4D). For C36c, correlation was weak at 0.18 under 0 mN/m applied surface tension and moderate at 0.42 under 10 mN/m tension. By contrast, weak tail-based interdigitation (λ_{OV}^{WEAK}) correlated poorly with APL, with Pearson coefficients of 0.39 (Drude), 0.29 (C36s), 0.32 (C36c 10 mN/m), and 0.09 (C36c 0 mN/m) (SI Fig. 2). These data support the conclusion that SURF-TG, not tail overlap, is the dominant contributor to monolayer expansion.

Collectively, our results are consistent with past work demonstrating that SURF-TGs promote monolayer expansion, and that applied surface tension further enhances SURF-TG interdigitation and expansion (67). While the C36s force field overestimates the magnitude of increased intercalation in response to applied surface tension, the Drude simulations demonstrate the same underlying trend at magnitudes more consistent with experimental expectations. This supports the physical mechanism proposed previously, while providing a more accurate representation grounded in polarization-responsive force field behavior. Nonetheless, the C36s model remains a useful approximation at 0 mN/m, where its predicted expansion and SURF-TG levels closely match those observed in Drude and experiment.

Core Hydration: We then evaluated hydration levels of the LD systems. When both Drude and C36c systems were initiated from the same C36s-equilibrated configuration, they expelled excess water from the core, reducing hydration from ~0.06 g/cm³ to ~0.001 g/cm³—matching experimental estimates (Fig. 4C). This outcome in C36c is expected and has previously been demonstrated (12) given its reduced glycerol charges and resulting increased core hydrophobicity. Notably, the Drude system exhibited the same degree of dehydration, suggesting that although SURF-TGs remain surface-active, the polarizable model appropriately limits water retention in the LD core. This behavior arises from the ability of Drude-induced dipoles to dynamically adjust to the low-polarity interior, suppressing glycerol–water interactions within the core while preserving interfacial activity at the monolayer. This balance between interfacial water engagement and core water exclusion is critical for accurately capturing LD physical properties and maintaining biologically realistic behavior.

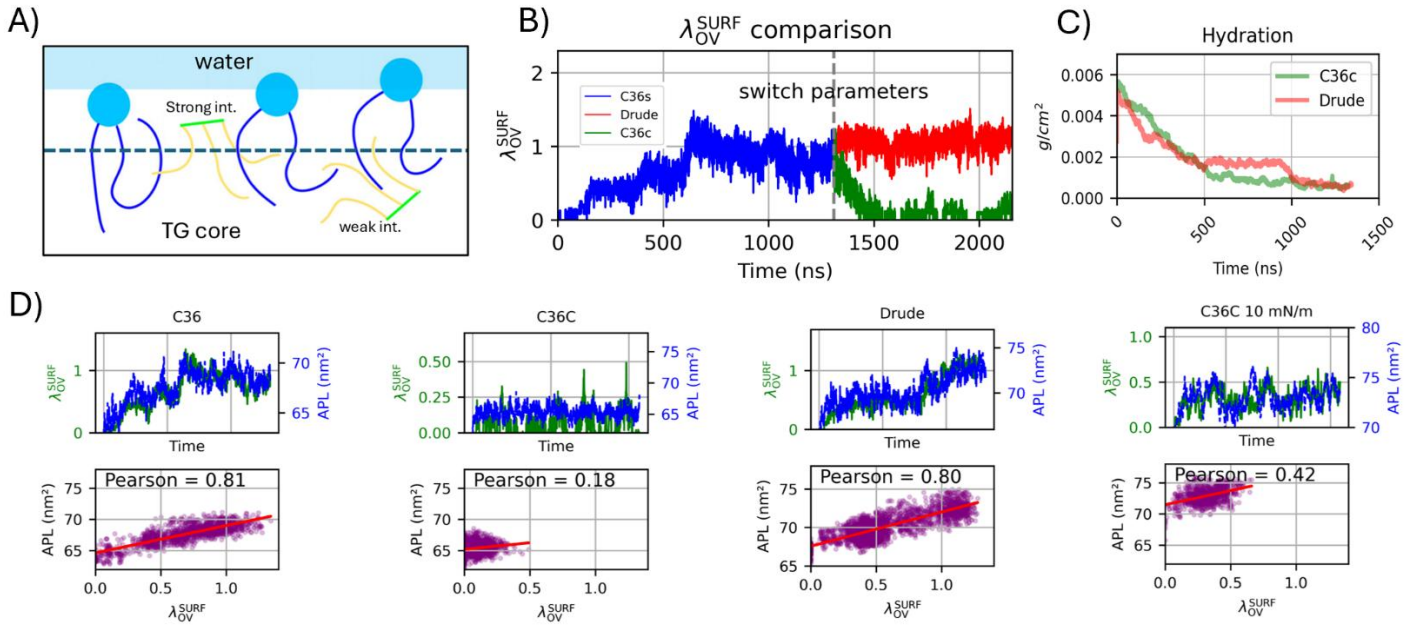


Figure 4. (A) SURF-TG are TG that rise to the LD monolayer surface and behave as membrane components, effectively expanding the LD monolayer. (B) λ_{OV}^{SURF} starting from the C36s equilibrated LD system (blue), then switching to Drude (red) and C36c (green). λ_{OV}^{SURF} is measured in units of nm is used to measure the magnitude of overlap of SURF-TG. For reference, a value of 1 nm would be approximately 12 SURF-TG per 270 PLs, while 0.2 nm would be approximately 1 SURF-TG. (C) The hydration of the Drude and C36c LD cores decreases down to experimental values (0.001 g/cm^3). (D) The λ_{OV}^{SURF} correlates with the APL, indicating that the SURF-TG are in part responsible for the LD APL expansion when compared to the ER bilayer.

Stability and Lifetime of SURF-TGs at the Drude LD Monolayer-Water Interface: To assess the stability of SURF-TG within the LD monolayer, we calculated the potential of mean force (PMF) for TG headgroup positions relative to the PL interface. Specifically, we measured the z-position of the sn-2 carbon of the TG glycerol backbone relative to the PL C2 atom, located just below the PL headgroup. The PMF was obtained from the equilibrium probability distribution using the Boltzmann relation: $G(z) = -k_B T \ln p(z)$, where $p(z)$ is the probability density of observing the glycerol at position z (Fig. 5A–D). Among all models, the Drude force field showed the strongest interfacial stabilization of TGs. The free energy difference between the SURF-TG minimum near the PL region and the bulk TG phase was 1.14 ± 0.09 kcal/mol for Drude, compared to 1.41 ± 0.05 kcal/mol for C36s and 1.66 ± 0.02 kcal/mol for C36c at 10 mN/m (SI Fig 3). In addition, Drude exhibited the highest barrier for SURF-TGs to return to the LD core (1.23 ± 0.09 kcal/mol), consistent with our observations that TGs at the interface are retained for longer times. This likely results from favorable interactions with water at the interface and avoidance of the hydrophobic PL tail region below. However, Drude also had the largest barrier to monolayer entry (2.59 ± 0.55 kcal/mol), consistent with the slower equilibration times for Drude. In contrast, C36s TGs showed a lower return barrier of 0.4 ± 0.35 kcal/mol and an entry barrier of 1.72 ± 0.32 kcal/mol. The C36c system at 10 mN/m exhibited the weakest interfacial stabilization, with a return barrier of only 0.05 ± 0.12 kcal/mol and a shallow entry barrier of 1.82 ± 0.10 kcal/mol. Notably, the C36c system at 0 mN/m displayed no energy minimum in the PL headgroup region, consistent with the near-complete absence of SURF-TGs in that environment (Fig. 5B). This plateau-like energy landscape explains the rapid diffusion of TGs away from the interface and poor retention in C36c even with 10 mN/m of applied surface tension.

To connect the PMF to dynamic behavior, we quantified SURF-TG residence times at the interface. A buffered classification scheme was implemented to reduce noise from transient fluctuations. TGs were considered surface-associated if, despite briefly dipping below the z-cutoff (average midplane center-of-mass within a 200 ps window), they retained at least four glycerol oxygens above the threshold. Using this approach, we found that Drude LDs had the longest SURF-TG lifetimes with an average of 5.3 ns, followed by C36s at 3.5 ns. C36c LDs at 10 mN/m showed markedly shorter lifetimes, averaging just 0.8 ns (full distribution in Fig. 5E). Together, the PMF and lifetime results demonstrate that the Drude force field not only stabilizes TGs at the monolayer interface more

effectively than C36s or C36c, but also significantly prolongs their residence time. The weak interfacial stabilization and rapid diffusion observed in the C36c system—particularly under physiological surface tension—are consistent with its lack of a defined free energy minimum in the PL headgroup region. These findings are further illustrated in Movie 1, which shows SURF-TG dynamics over a 20 ns window for all systems.

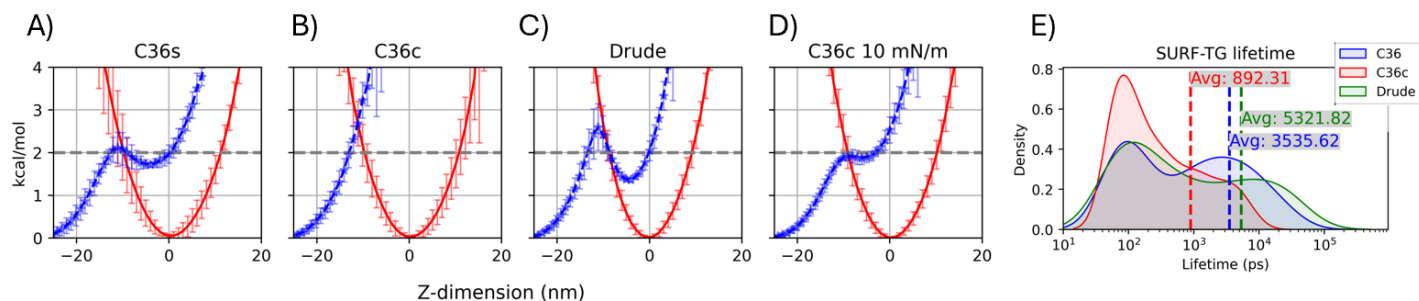


Figure 5. (A-D) PMF of SURF-TGs along the z-dimension (blue) with respect to the PL C2 atoms (red). (E) Distribution and average SURF-TG lifetimes.

Membrane Behavior of SURF-TG: To compare the dynamic structural behavior of SURF-TGs within the monolayer, we quantified the orientation and ordering of their acyl tails relative to the glycerol headgroup using vector-based order parameters. These parameters reflect tail splaying, with lower values indicating greater dispersion and higher values corresponding to tighter alignment. Vectors were defined from the center of mass of the glycerol group to the terminal carbon atoms of each TG tail (C1–C3 in Fig. 6A), and cosine alignment with the z-axis was calculated. Among the models, Drude exhibited the highest average order parameter (0.74), followed by C36s (0.66) and C36c at 10 mN/m (0.58) (Fig. 6B–C). These values suggest that in Drude monolayers, TG headgroups are more consistently oriented toward the aqueous phase with tails extending downward, aligning with the monolayer PLs. C36s shows similar behavior, but with more variation over time (Fig. 6B), while C36c exhibits the greatest lateral splaying of tails at 10 mN/m. The order parameter distributions (Fig. 6C) further reflect these differences. Drude forms a single, skewed Gaussian peak, while both C36s and C36c at 10 mN/m exhibit a secondary peak near zero (90°), indicating increased stabilization of conformations with greater lateral tail mobility. This behavior arises predominantly from two TG tails splaying upward, as shown in Fig. 6G and SI Fig. 4. The TG tails in these systems also display greater orientation variability and shorter cosine alignment autocorrelation times (Fig. 6F), whereas Drude TGs maintain more persistent orientation and slower relaxation, indicative of reduced dynamical reorientation. These trends are consistent with the dynamics displayed in Movie 1.

To assess whether SURF-TGs behave comparably to phospholipid components of the membrane, we calculated the carbon-deuterium order parameter (S_{CD}) along the TG acyl chains and DOPE lipids. All models produced similar SURF-TG ordering profiles to those observed for DOPE, with the Drude model showing greater order in the upper tail region but increased disorder in the lower tail (Fig. 6D,E). This pattern is consistent with previous observations of Drude-modeled unsaturated lipids, including DOPE (35). To see how applied surface tension influences the PL tail order we extended this comparison for DOPE lipids to C36c at 5 and 10 mN/m. As anticipated, increasing surface tension in the C36c monolayer reduces tail order (Fig. 6E). Although Drude shows higher cosine alignment of SURF-TG tails, it has lower S_{CD} values in the lower tail region compared to fixed-charge models (Fig. 6C–E). This is because S_{CD} reflects local C–H bond orientation, not overall tail direction (68). Drude tails are more vertically aligned, but greater torsional flexibility at the tail end reduces S_{CD} .

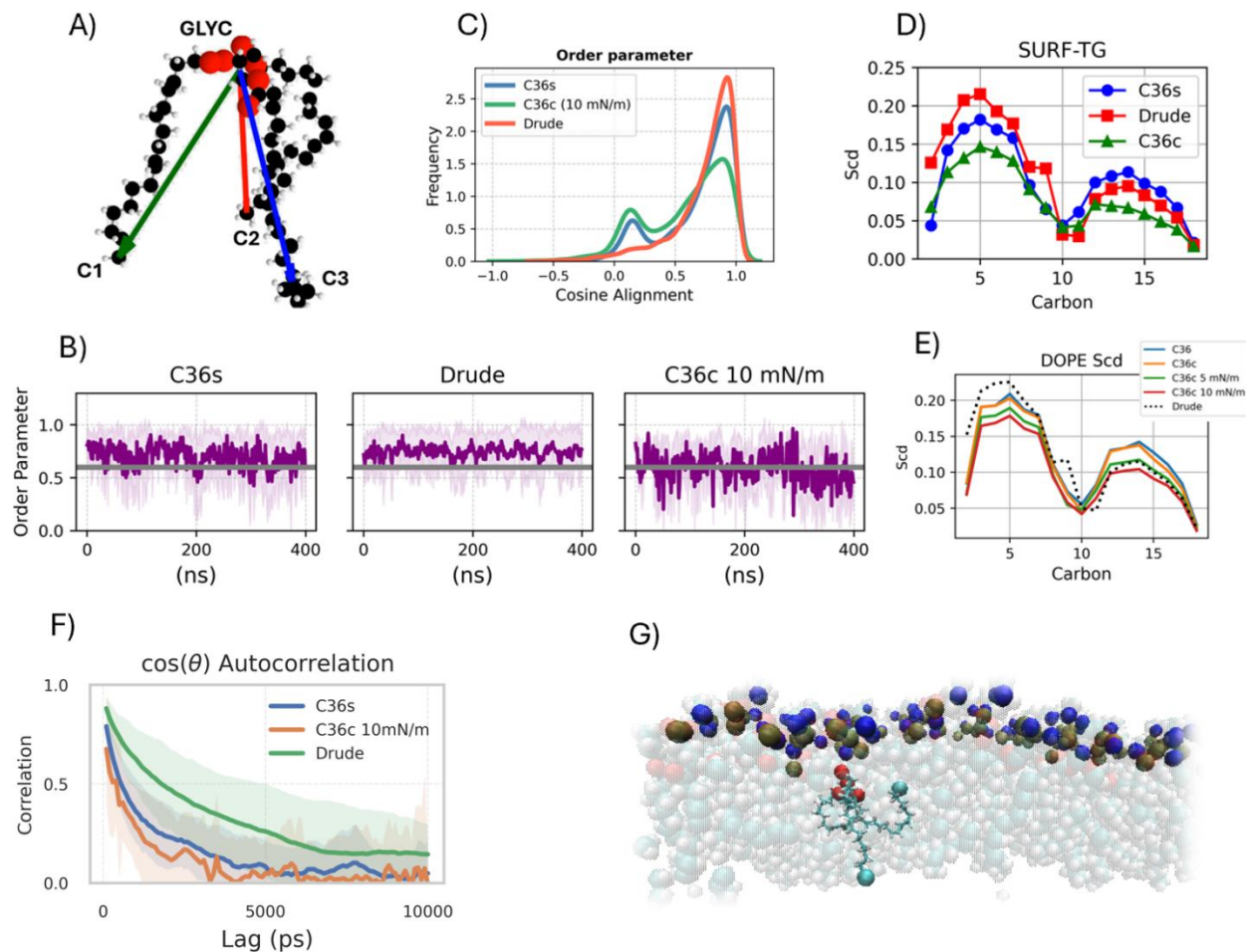


Figure 6. (A) Vectors of GLYC to C1-C3 are used to measure the cosine alignment of the SURF-TG tails. (B) TG cosine alignment as a function of time and (C) full distribution. (D) Tail order parameters (S_{CD}) for the SURF-TG and (E) DOPE PLs. (F) Autocorrelation for cosine alignment of the TG tails for the various LD systems. (G) Representative structure from C36s and C36c cosine alignment peak approximately at 0.1 showing more prominent disordered SURF-TG tails. The glycerol oxygen atoms and ends of the tails are represented by red and cyan beads, respectively.

Drude Demonstrates Chemically-Distinct Packing Defects: Packing defects at the LD surface are critical sites for protein binding and reflect underlying differences in monolayer organization. To evaluate how force field choice influences defect structure, we quantified three distinct defect types: PL-acyl defects (exposed phospholipid tails), TG-acyl defects (exposed TG tails), and TG-glycerol (TG-glyc) defects (exposed TG headgroups), as illustrated in Fig. 7A–B. These features provide insight into the degree of surface disorder and the types of chemical groups accessible for protein interaction. When examining the distribution of defect sizes, PL-acyl defect probabilities remained relatively similar across systems, with C36c at 10 mN/m showing a distinguishable increase (Fig. 7C). In contrast, TG-induced defects clearly varied across models. We further analyzed the frequency of defects ($>15 \text{ \AA}^2$) per frame to better distinguish structural differences (Fig. 7D–E). C36c at 10 mN/m exhibited the highest number of PL-acyl defects (~ 40 per frame), indicating increased phospholipid tail exposure under tension. Drude and C36s showed comparable PL-acyl defect counts (~ 31 and 30 /frame, respectively), while C36c at 0 mN/m had slightly fewer (~ 27 /frame). Notably, Drude and C36s exhibited far greater numbers of TG-glyc defects (~ 6.4 /frame), whereas C36c systems showed minimal TG-glyc defects at 0 mN/m (~ 0.1 /frame), increasing only modestly under tension (~ 1.9 /frame at 10 mN/m). Similarly, Drude and C36s showed 2.2 and 4.2 TG-acyl defects per frame, respectively, while C36c produced fewer (0.5 at 0 mN/m and 3.1 at 10 mN/m).

These results suggest that Drude and C36s monolayers present similar surface properties that are distinct from C36c. With a more TG-rich defect landscape, Drude and C36s have exposed glycerol regions that potentially

provide unique binding motifs for LD-targeting proteins over PL bilayers. In contrast, C36c at 0 mN/m exhibits a compact monolayer with few accessible TG groups. In response to 10 mN/m surface tension, C36c presents an inverted defect profile, characterized by a shift toward PL-acyl exposure and reduced TG-glyc presentation (Fig. 7 D,E). This increase in PL tail exposure is more similar to bilayers under tension than LD surfaces with chemically-distinct packing defects.

While future studies should verify the role of different TG forcefields on polar interactions with embedded proteins, the results herein suggest polar interactions that would stabilize C36s and Drude would be lost in C36c. The Drude model, which exhibited strong SURF-TG alignment and retention, also presents a consistent and biologically relevant surface defect profile, suggesting stable integration of TGs into the monolayer. This integration may not only influence local lipid structure but also contribute to the mechanical and dynamic properties of the LD interface, potentially modulating how the surface responds to protein recruitment, membrane remodeling, and stress.

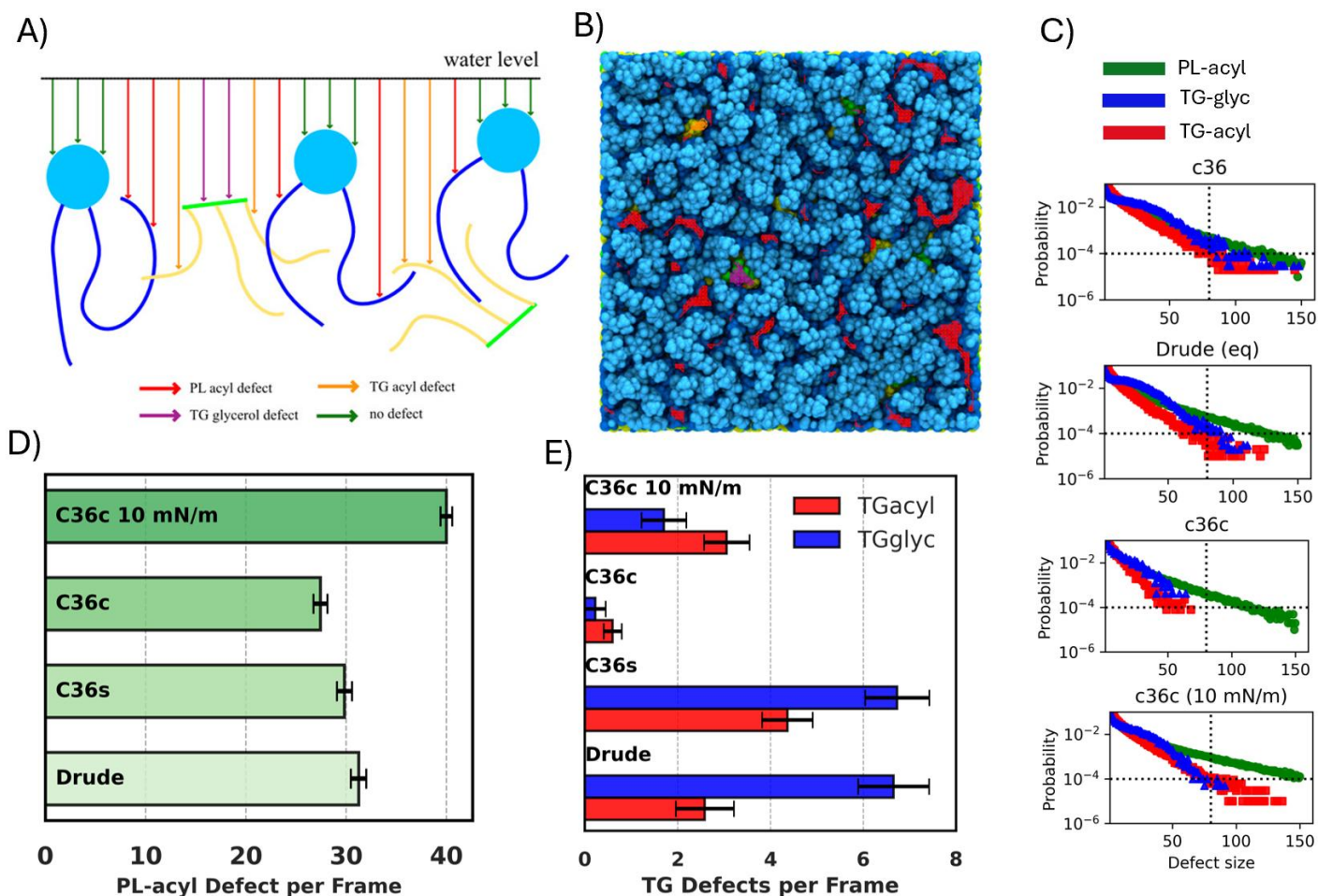


Figure 7. (A) The different types of packing defects are chemically unique depending if they are induced from PL-acyls, TG-acyls, or TG-glycerols. (B) The birds-eye view the the membrane defects. Red is PL-acyl, purple is TG-glycerol, and orange is TG-acyl. (C) Plots representing the defect size vs. probability. (D) Frequency of PL-acyl defects, and (E) frequency of TG-acyl and TG-glyc defects.

Core TG Diffusivity and Glycerol Interactions: To understand how force field choice influences TG dynamics within the LD core, we computed the three-dimensional mean-squared displacement (3D-MSD) of TG molecules (Fig. 8A). The C36c LD at 0 mN/m exhibited the highest diffusivity, with TGs diffusing ~25% faster than in the C36s model. Interestingly, increasing the surface tension to 10 mN/m in C36c slightly reduced diffusion in the core by ~11%, likely due to increased tail intercalation (Fig. SI 2). In contrast, the Drude LD showed significantly slower TG dynamics (~67.8% slower than C36c at 0 mN/m and ~56.7% slower than C36s) indicating markedly reduced mobility in the polarizable system. Slower yet more accurate diffusion behavior for PLs has previously been

reported for systems modeled with the Drude force field (35, 37, 69). To determine whether these differences stem from dipole effects or specific glycerol–glycerol interactions, we analyzed intermolecular structure using radial distribution functions (RDFs). RDFs calculated for TG headgroup atoms, specifically the glycerol oxygens (Fig. 8C) and carbons (Fig. 8D), showed more pronounced peaks in the C36s and Drude models, indicating stronger short-range ordering and closer headgroup association. The Drude model exhibited the strongest peaks, indicating a high degree of short-range structuring and stronger glycerol–glycerol association. Despite C36s being overly polar, it is less structured, indicating less long-lived TG-TG interactions in the core, than Drude. As expected, the C36c system showed weaker peaks, reflecting looser packing and less cohesive headgroup interactions. RDFs calculated for TG acyl tail ends (Fig. 8B) were nearly identical across all systems, confirming that the observed differences in diffusion are driven by interactions at the glycerol headgroups rather than tail behavior. These findings demonstrate that the reduced diffusivity observed in the Drude model arises from polarization-enhanced glycerol–glycerol interactions, which restrict TG mobility in the LD core.

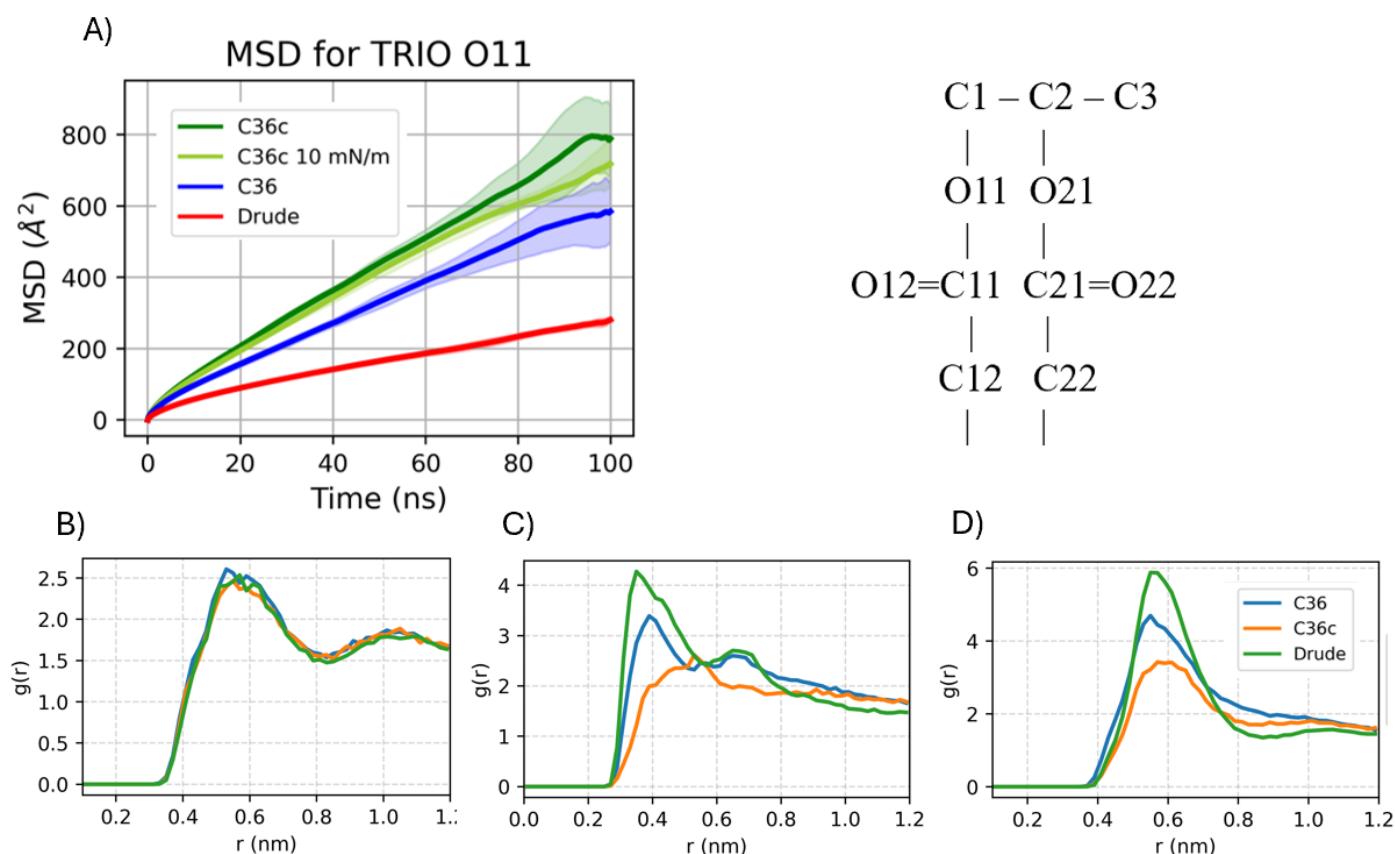


Figure 8. (A) The MSD of LD core-TG of the the varying LD systems. (B) RDF profiles of the C316 (tail), (C) O11, and (D) C2 glycerol atoms of the core-TG in the different LD systems.

Conclusions

LD simulations depend on a balance of interactions between neutral lipids, PLs, water, and interacting substrates, including proteins. Accordingly, neutral lipid force fields must reflect this balance in both the hydrophobic LD core and the polar PL monolayer interface. The fixed charge force fields used to date for TG, the dominant neutral lipid in LDs, have been successful in capturing either bulk hydration and the water-TG interfacial tension with smaller partial charges on glycerol (more hydrophobic) or LD monolayer expansion with larger partial charges (more polar). But no forcefield (CG or all atom) has been able to capture all of the available experimental parameters, as summarized in Table 1. Herein we tested the impact of adding polarizability via the Drude2023 lipid forcefield to enable a dynamic charge distribution that responds to polar and hydrophobic interactions. Building parameters from glycerol and DOPE tails, we find that the Drude2023 TG model reproduces the experimental properties,

including bulk TG density, the bare TG–water interfacial tension, LD monolayer expansion, and core hydration (based on the hydration of bulk olive oil).

In comparison, C36s overestimates core hydration and underestimates the bare water-TG interfacial tension, while C36c requires a large applied surface tension to reproduce experimental monolayer expansion. Despite its shortcomings, C36s run in the NPT ensemble closely reproduces the experimentally measured LD-to-bilayer expansion ratio and replicates the surface properties (% SURF-TG, magnitude and type of packing defects, SURF-TG free energy profile) demonstrated by the Drude model, making it more suitable for studies focused on the LD monolayer and protein-monomolayer interactions.

Conversely, C36c better represents the TG–water interfacial tension and low LD core hydration, making it more suitable for studies focused on the bare water-TG interface, or when core hydration properties matter. Capturing the expansion behavior of the C36c LD requires the application of ~ 10 mN/m surface tension, which is far larger than the experimentally measured surface tension of ~ 1 -3 mN/m. Once applied, however, the properties of the monolayer are not consistent with the Drude model, showing more transient SURF-TG with floppy tails and a dominance of tail intercalation and PL acyl defects. Differences are also apparent in the core properties where the Drude model shows slower diffusion and more pronounced glycerol-glycerol interactions than C36s and much more significantly than C36c. Thus, the polarizable Drude model emerges as the most experimentally consistent choice, effectively capturing bulk TG density, interfacial tension, monolayer expansion, and LD core hydration without requiring non-physiological surface tensions.

Overall, forcefield selection should reflect the simulation's primary goal, whether prioritizing surface properties or core hydration. Importantly, there remains a need to experimentally resolve the composition of the LD monolayer. While earlier studies have addressed this question in the context of lipoproteins (28, 65, 66), direct evidence for LDs is still lacking. We are optimistic that modern neutron and X-ray scattering techniques, combined with our simulated electron density profiles (SI Fig. 5), can be used to fit and interpret future experimental data through calculated form factors, as was done in earlier work (70–72). Such an approach could offer a more definitive means of identifying the presence of SURF-TG at the LD interface, and benchmarking forcefields. Additionally, future work should investigate experimental measurements of the LD core hydration, how protein interactions with the LD monolayer are altered by polarization, and if it is possible to develop improved fixed-charge models.

Supporting Information

Additional analyses including weak TG–PL interdigitation, potential of mean force (PMF) profiles, SURF-TG orientation distributions, and electron density decompositions across lipid droplet monolayers (PDF); Movie 1 demonstrates SURF-TG dynamics highlighting the surface-oriented TG at the beginning of this 2.5 ns section of the trajectory. For C36c all transition to the core. For C36s, one is initially transferring and another transitions midway though. None transition for Drude. (MP4)

Acknowledgements

The authors are grateful to Richard Pastor and Jeff Klauda for insightful discussions, and extend special thanks to Richard Venable for his valuable guidance and assistance with CHARMM scripting. The work was supported by the National Science Foundation under Grant No. (2341008) and the computational resources provided by Expanse through the San Diego Supercomputer through the Center Advanced Cyberinfrastructure Coordination Ecosystem (ACCESS) program (allocation MCB200018) supported by NSF (grant nos. 2138259, 2138286, 2138307, 2137603, and 2138296), as well as the Center for High-Performance Computing (CHPC) at the University of Utah. These resources greatly aided in the completion of this research.

Author contributions

R.J.B and J.M.J.S designed the research. R.J.B. ran the simulations and analyzed the results. J.M.J.S directed the research. Both authors wrote the manuscript and agreed on the final version.

Competing interests

The authors declare no competing interests.

References

1. Walther, T.C., J. Chung, and R. V Farese. 2017. Lipid Droplet Biogenesis. *Annu Rev Cell Dev Biol.*
2. Zhang, C., and P. Liu. 2019. The New Face of the Lipid Droplet: Lipid Droplet Proteins. *Proteomics.* 19.
3. Olarte, M.J., J.M.J. Swanson, T.C. Walther, and R. V. Farese. 2021. The CYTOLD and ERTOLD pathways for lipid droplet–protein targeting. *Trends Biochem Sci.*
4. Bersuker, K., and J.A. Olzmann. 2017. Establishing the lipid droplet proteome: Mechanisms of lipid droplet protein targeting and degradation. *Biochim Biophys Acta Mol Cell Biol Lipids.* 1862:1166–1177.
5. Sapia, J., and S. Vanni. 2024. Molecular dynamics simulations of intracellular lipid droplets: a new tool in the toolbox. *FEBS Lett.* 598:1143–1153.
6. Kim, S., J.M.J. Swanson, and G.A. Voth. 2022. Computational Studies of Lipid Droplets. *Journal of Physical Chemistry B.* 126:2145–2154.
7. Marrink, S.J., V. Corradi, P.C.T. Souza, H.I. Ingólfsson, D.P. Tieleman, and M.S.P. Sansom. 2019. Computational Modeling of Realistic Cell Membranes. *Chem Rev.* 119:6184–6226.
8. Venable, R.M., A. Krämer, and R.W. Pastor. 2019. Molecular Dynamics Simulations of Membrane Permeability. *Chem Rev.* 119:5954–5997.
9. Leonard, A.N., E. Wang, V. Monje-Galvan, and J.B. Klauda. 2019. Developing and Testing of Lipid Force Fields with Applications to Modeling Cellular Membranes. *Chem Rev.* 119:6227–6269.
10. Pluhackova, K., S.A. Kirsch, J. Han, L. Sun, Z. Jiang, T. Unruh, and R.A. Böckmann. 2016. A Critical Comparison of Biomembrane Force Fields: Structure and Dynamics of Model DMPC, POPC, and POPE Bilayers. *Journal of Physical Chemistry B.* 120:3888–3903.
11. Klauda, J.B., R.M. Venable, J.A. Freites, J.W. O'Connor, D.J. Tobias, C. Mondragon-Ramirez, I. Vorobyov, A.D. Mackerell, and R.W. Pastor. 2010. Update of the CHARMM All-Atom Additive Force Field for Lipids: Validation on Six Lipid Types. *Journal of Physical Chemistry B.* 114:7830–7843.
12. Campomanes, P., J. Prabhu, V. Zoni, and S. Vanni. 2021. Recharging your fats: CHARMM36 parameters for neutral lipids triacylglycerol and diacylglycerol. *Biophysical Reports.* 1:100034.
13. Kim, S., and G.A. Voth. 2021. Physical Characterization of Triolein and Implications for Its Role in Lipid Droplet Biogenesis. *Journal of Physical Chemistry B.* 125:6874–6888.
14. Chaban, V. V., and H. Khandelia. 2014. Lipid structure in triolein lipid droplets. *Journal of Physical Chemistry B.* 118:10335–10340.
15. Leontyev, I. V., M. V. Vener, I. V. Rostov, M. V. Basilevsky, and M.D. Newton. 2003. Continuum level treatment of electronic polarization in the framework of molecular simulations of solvation effects. *Journal of Chemical Physics.* 119:8024–8037.
16. Leontyev, I., and A. Stuchebrukhov. 2011. Accounting for electronic polarization in non-polarizable force fields. *Physical Chemistry Chemical Physics.* 13:2613–2626.
17. Leontyev, I. V., and A.A. Stuchebrukhov. 2010. Electronic Polarizability and the Effective Pair Potentials of Water. *J Chem Theory Comput.* 6:3153–3161.
18. Leontyev, I. V., and A.A. Stuchebrukhov. 2014. Polarizable molecular interactions in condensed phase and their equivalent nonpolarizable models. *Journal of Chemical Physics.* 141.

19. Leontyev, I. V., and A.A. Stuchebrukhov. 2009. Electronic continuum model for molecular dynamics simulations. *Journal of Chemical Physics*. 130.
20. Cerutti, D.S., J.E. Rice, W.C. Swope, and D.A. Case. 2013. Derivation of fixed partial charges for amino acids accommodating a specific water model and implicit polarization. *Journal of Physical Chemistry B*. 117:2328–2338.
21. Hermans, Jan., Ahammadunny. Pathiaseril, and Amil. Anderson. 1988. Excess free energy of liquids from molecular dynamics simulations. Application to water models. *J Am Chem Soc*. 110:5982–5986.
22. Jorge, M. 2017. Predicting hydrophobic solvation by molecular simulation: 2. New united-atom model for alkanes, alkenes, and alkynes. *J Comput Chem*. 38:359–369.
23. Jorge, M. 2024. Theoretically grounded approaches to account for polarization effects in fixed-charge force fields. *Journal of Chemical Physics*. 161.
24. Iuchi, S., S. Izvekov, and G.A. Voth. 2007. Are many-body electronic polarization effects important in liquid water? *J Chem Phys*. 126:124505.
25. Chen, S., and G.A. Voth. 2023. How Does Electronic Polarizability or Scaled-Charge Affect the Interfacial Properties of Room Temperature Ionic Liquids? *Journal of Physical Chemistry B*. 127:1264–1275.
26. Gouw, T.H., and J.C. Vlugter. 1966. Physical Properties of Triglycerides. I. Density and Refractive Index. *Fette, Seifen, Anstrichmittel*. 68:544–549.
27. Couallier, E., A. Riaublanc, E. David Briand, and B. Rousseau. 2018. Molecular simulation of the water-triolein-oleic acid mixture: Local structure and thermodynamic properties. *Journal of Chemical Physics*. 148.
28. Mitsche, M.A., L. Wang, and D.M. Small. 2010. Adsorption of egg phosphatidylcholine to an air/water and triolein/water bubble interface: Use of the 2-dimensional phase rule to estimate the surface composition of a phospholipid/triolein/water surface as a function of surface pressure. *Journal of Physical Chemistry B*. 114:3276–3284.
29. Ragni, L., A. Berardinelli, C. Cevoli, and E. Valli. 2012. Assessment of the water content in extra virgin olive oils by Time Domain Reflectometry (TDR) and Partial Least Squares (PLS) regression methods. *J Food Eng*. 111:66–72.
30. Chorlay, A., and A.R. Thiam. 2020. Neutral lipids regulate amphipathic helix affinity for model lipid droplets. *Journal of Cell Biology*. 219.
31. Chorlay, A., L. Forêt, and A.R. Thiam. 2021. Origin of gradients in lipid density and surface tension between connected lipid droplet and bilayer. *Biophys J*. 120:5491–5503.
32. Kim, S., and J.M.J. Swanson. 2020. The Surface and Hydration Properties of Lipid Droplets. *Biophys J*. 119:1958–1969.
33. Prévost, C., M.E. Sharp, N. Kory, Q. Lin, G.A. Voth, R. V. Farese, and T.C. Walther. 2018. Mechanism and Determinants of Amphipathic Helix-Containing Protein Targeting to Lipid Droplets. *Dev Cell*. 44:73-86.e4.
34. Olarte, M.J., S. Kim, M.E. Sharp, J.M.J. Swanson, R. V. Farese, and T.C. Walther. 2020. Determinants of Endoplasmic Reticulum-to-Lipid Droplet Protein Targeting. *Dev Cell*. 54:471-487.e7.
35. Yu, Y., R.M. Venable, J. Thirman, P. Chatterjee, A. Kumar, R.W. Pastor, B. Roux, A.D. MacKerell, and J.B. Klauda. 2023. Drude Polarizable Lipid Force Field with Explicit Treatment of Long-Range Dispersion: Parametrization and Validation for Saturated and Monounsaturated Zwitterionic Lipids. *J Chem Theory Comput*. 19:2590–2605.
36. Chowdhary, J., E. Harder, P.E.M. Lopes, L. Huang, A.D. MacKerell, and B. Roux. 2013. A polarizable force field of dipalmitoylphosphatidylcholine based on the classical drude model for molecular dynamics simulations of lipids. *Journal of Physical Chemistry B*. 117:9142–9160.

37. Li, H., J. Chowdhary, L. Huang, X. He, A.D. MacKerell, and B. Roux. 2017. Drude Polarizable Force Field for Molecular Dynamics Simulations of Saturated and Unsaturated Zwitterionic Lipids. *J Chem Theory Comput.* 13:4535–4552.
38. Lyu, X., J. Wang, J. Wang, Y.S. Yin, Y. Zhu, L.L. Li, S. Huang, S. Peng, B. Xue, R. Liao, S.Q. Wang, M. Long, T. Wohland, B.T. Chua, Y. Sun, P. Li, X.W. Chen, L. Xu, F.J. Chen, and P. Li. 2021. A gel-like condensation of Cidec generates lipid-permeable plates for lipid droplet fusion. *Dev Cell.* 56:2592–2606.e7.
39. Thiam, A.R., R. V. Farese, and T.C. Walther. 2013. The biophysics and cell biology of lipid droplets. *Nat Rev Mol Cell Biol.* 14:775–786.
40. Irving, J.H., and J.G. Kirkwood. 1950. The Statistical Mechanical Theory of Transport Processes. IV. The Equations of Hydrodynamics. *J Chem Phys.* 18:817–829.
41. Eastman, P., J. Swails, J.D. Chodera, R.T. McGibbon, Y. Zhao, K.A. Beauchamp, L.P. Wang, A.C. Simmonett, M.P. Harrigan, C.D. Stern, R.P. Wiewiora, B.R. Brooks, and V.S. Pande. 2017. OpenMM 7: Rapid development of high performance algorithms for molecular dynamics. *PLoS Comput Biol.* 13.
42. Lamoureux, G., E. Harder, I. V. Vorobyov, B. Roux, and A.D. MacKerell. 2006. A polarizable model of water for molecular dynamics simulations of biomolecules. *Chem Phys Lett.* 418:245–249.
43. Wennberg, C.L., T. Murtola, B. Hess, and E. Lindahl. 2013. Lennard-Jones lattice summation in bilayer simulations has critical effects on surface tension and lipid properties. *J Chem Theory Comput.* 9:3527–3537.
44. Brooks, B.R., C.L. Brooks, A.D. Mackerell, L. Nilsson, R.J. Petrella, B. Roux, Y. Won, G. Archontis, C. Bartels, S. Boresch, A. Caflisch, L. Caves, Q. Cui, A.R. Dinner, M. Feig, S. Fischer, J. Gao, M. Hodoscek, W. Im, K. Kuczera, T. Lazaridis, J. Ma, V. Ovchinnikov, E. Paci, R.W. Pastor, C.B. Post, J.Z. Pu, M. Schaefer, B. Tidor, R.M. Venable, H.L. Woodcock, X. Wu, W. Yang, D.M. York, and M. Karplus. 2009. CHARMM: The biomolecular simulation program. *J Comput Chem.* 30:1545–1614.
45. Braun, R.J., and J.M.J. Swanson. 2022. Capturing the Liquid-Crystalline Phase Transformation: Implications for Protein Targeting to Sterol Ester-Rich Lipid Droplets. *Membranes (Basel).* 12.
46. Lee, J., X. Cheng, J.M. Swails, M.S. Yeom, P.K. Eastman, J.A. Lemkul, S. Wei, J. Buckner, J.C. Jeong, Y. Qi, S. Jo, V.S. Pande, D.A. Case, C.L. Brooks, A.D. MacKerell, J.B. Klauda, and W. Im. 2016. CHARMM-GUI Input Generator for NAMD, GROMACS, AMBER, OpenMM, and CHARMM/OpenMM Simulations Using the CHARMM36 Additive Force Field. *J Chem Theory Comput.* 12:405–413.
47. Jo, S., T. Kim, V.G. Iyer, and W. Im. 2008. CHARMM-GUI: A web-based graphical user interface for CHARMM. *J Comput Chem.* 29:1859–1865.
48. Martinez, L., R. Andrade, E.G. Birgin, and J.M. Martínez. 2009. PACKMOL: A package for building initial configurations for molecular dynamics simulations. *J Comput Chem.* 30:2157–2164.
49. Abraham, M.J., T. Murtola, R. Schulz, S. Páll, J.C. Smith, B. Hess, and E. Lindahl. 2015. Gromacs: High performance molecular simulations through multi-level parallelism from laptops to supercomputers. *SoftwareX.* 1–2:19–25.
50. Huang, J., S. Rauscher, G. Nawrocki, T. Ran, M. Feig, B.L. De Groot, H. Grubmüller, and A.D. MacKerell. 2016. CHARMM36m: An improved force field for folded and intrinsically disordered proteins. *Nat Methods.* 14:71–73.
51. Nosé, S. 1984. A unified formulation of the constant temperature molecular dynamics methods. *J Chem Phys.* 81:511–519.
52. Essmann, U., L. Perera, M.L. Berkowitz, T. Darden, H. Lee, and L.G. Pedersen. 1995. A smooth particle mesh Ewald method. *J Chem Phys.* 103:8577–8593.
53. Parrinello, M., and A. Rahman. 1981. Polymorphic transitions in single crystals: A new molecular dynamics method. *J Appl Phys.* 52:7182–7190.
54. Hess, B. 2008. P-LINCS: A parallel linear constraint solver for molecular simulation. *J Chem Theory Comput.* 4:116–122.

55. Berendsen, H.J.C., J.P.M. Postma, W.F. Van Gunsteren, A. Dinola, and J.R. Haak. 1984. Molecular dynamics with coupling to an external bath. *J Chem Phys.* 81:3684–3690.
56. Bacle, A., R. Gautier, C.L. Jackson, P.F.J. Fuchs, and S. Vanni. 2017. Interdigitation between Triglycerides and Lipids Modulates Surface Properties of Lipid Droplets. *Biophys J.* 112:1417–1430.
57. Das, C., M.G. Noro, and P.D. Olmsted. 2009. Simulation studies of stratum corneum lipid mixtures. *Biophys J.* 97:1941–1951.
58. Schindler, H., and J. Seelig. 1975. Deuterium Order Parameters in Relation to Thermodynamic Properties of a Phospholipid Bilayer. A Statistical Mechanical Interpretation[^]. .
59. Gautier, R., A. Bacle, M.L. Tiberti, P.F. Fuchs, S. Vanni, and B. Antonny. 2018. PackMem: A Versatile Tool to Compute and Visualize Interfacial Packing Defects in Lipid Bilayers. *Biophys J.* 115:436–444.
60. Cui, H., E. Lyman, and G.A. Voth. 2011. Mechanism of membrane curvature sensing by amphipathic helix containing proteins. *Biophys J.* 100:1271–1279.
61. Vanni, S., L. Vamparys, R. Gautier, G. Drin, C. Etchebest, P.F.J. Fuchs, and B. Antonny. 2013. Amphipathic lipid packing sensor motifs: Probing bilayer defects with hydrophobic residues. *Biophys J.* 104:575–584.
62. de Buyl, P. 2018. tidynamics: A tiny package to compute the dynamics of stochastic and molecular simulations. *J Open Source Softw.* 3:877.
63. Calandrini, V., E. Pellegrini, P. Calligari, K. Hinsén, and G.R. Kneller. 2011. nMoldyn - Interfacing spectroscopic experiments, molecular dynamics simulations and models for time correlation functions. *École thématique de la Société Française de la Neutronique.* 12:201–232.
64. Gowers, R.J., M. Linke, J. Barnoud, T.J. E Reddy, M.N. Melo, S.L. Seyler, J. Dománski, D.L. Dotson, S. Buchoux, I.M. Kenney, and O. Beckstein. 2016. MDAnalysis: A Python Package for the Rapid Analysis of Molecular Dynamics Simulations. .
65. Miller, K.W., and D.M. Small. 1983. Surface-to-Core and Interparticle Equilibrium Distributions of Triglyceride-rich Lipoprotein Lipids*. .
66. Mitsche, M.A., and D.M. Small. 2011. C-terminus of apolipoprotein A-I removes phospholipids from a triolein/phospholipids/water interface, but the N-terminus does not: A possible mechanism for nascent HDL assembly. *Biophys J.* 101:353–361.
67. Kim, S., M.I. Oh, and J.M.J. Swanson. 2021. Stressed Lipid Droplets: How Neutral Lipids Relieve Surface Tension and Membrane Expansion Drives Protein Association. *Journal of Physical Chemistry B.* 125:5572–5586.
68. Piggot, T.J., J.R. Allison, R.B. Sessions, and J.W. Essex. 2017. On the Calculation of Acyl Chain Order Parameters from Lipid Simulations. *J Chem Theory Comput.* 13:5683–5696.
69. Venable, R.M., A.J. Pane, A. Rice, and R.W. Pastor. 2025. Effects of a Polarizable Force Field on Membrane Dynamics: Surface Viscosity, Lipid Diffusion, and Peptide Induced Pore Formation. *J Comput Chem.* 46:e70001.
70. Kinnun, J.J., H.L. Scott, R. Ashkar, and J. Katsaras. 2021. Biomembrane Structure and Material Properties Studied With Neutron Scattering. *Front Chem.* 9.
71. Kučerka, N., J.F. Nagle, J.N. Sachs, S.E. Feller, J. Pencier, A. Jackson, and J. Katsaras. 2008. Lipid bilayer structure determined by the simultaneous analysis of neutron and X-ray scattering data. *Biophys J.* 95:2356–2367.
72. Klauda, J.B., N. Kučerka, B.R. Brooks, R.W. Pastor, and J.F. Nagle. 2006. Simulation-based methods for interpreting x-ray data from lipid bilayers. *Biophys J.* 90:2796–2807.

For Table of Contents Only

Interfacial polarization

